nanomaterials

MDPI

Article

Impact of Local Composition on the Emission Spectra of InGaN Quantum-Dot LEDs

Daniele Barettin [1,*], Alexei V. Sakharov [2], Andrey F. Tsatsulnikov [2], Andrey E. Nikolaev [2], Alessandro Pecchia [3], Matthias Auf der Maur [4,*], Sergey Yu. Karpov [5] and Nikolay Cherkashin [6]

1 Department of Electronic Engineering, Università Niccoló Cusano, 00133 Rome, Italy
2 Ioffe Physico-Technical Institute RAS, 26 Polytekhnicheskaya str., 194021 St. Petersburg, Russia; val.beam@mail.ioffe.ru (A.V.S.); andrew@beam.ioffe.ru (A.F.T.); Aen@mail.ioffe.ru (A.E.N.)
3 CNR-ISMN, Via Salaria Km. 29.300, Monterotondo, 00017 Rome, Italy; alessandro.pecchia@cnr.it
4 Department of Electronic Engineering, University of Rome Tor Vergata, Via del Politecnico 1, 00133 Rome, Italy
5 Soft-Impact, Ltd., P.O. Box 83, 27 Engels ave., 194156 St. Petersburg, Russia
6 CEMES-CNRS and Université de Toulouse, 29 rue Jeanne Marvig, BP 94347, F-31055 Toulouse, CEDEX 4, France
* Correspondence: daniele.barettin@unicusano.it (D.B.); auf.der.maur@ing.uniroma2.it (M.A.d.M.)

Abstract: A possible solution for the realization of high-efficiency visible light-emitting diodes (LEDs) exploits InGaN-quantum-dot-based active regions. However, the role of local composition fluctuations inside the quantum dots and their effect of the device characteristics have not yet been examined in sufficient detail. Here, we present numerical simulations of a quantum-dot structure restored from an experimental high-resolution transmission electron microscopy image. A single InGaN island with the size of ten nanometers and nonuniform indium content distribution is analyzed. A number of two- and three-dimensional models of the quantum dot are derived from the experimental image by a special numerical algorithm, which enables electromechanical, continuum $\vec{k} \cdot \vec{p}$, and empirical tight-binding calculations, including emission spectra prediction. Effectiveness of continuous and atomistic approaches are compared, and the impact of InGaN composition fluctuations on the ground-state electron and hole wave functions and quantum dot emission spectrum is analyzed in detail. Finally, comparison of the predicted spectrum with the experimental one is performed to assess the applicability of various simulation approaches.

Keywords: quantum dots; $\vec{k} \cdot \vec{p}$; empirical tight-binding; modeling

Citation: Barettin , D.; Sakharov, A.V.; Tsatsulnikov, A.F.; Nikolaev, A.E.; Pecchia, A.; Auf der Maur, M.; Karpov, S.Y.; Cherkashin, N. Impact of Local Composition on the Emission Spectra of InGaN Quantum-Dot LEDs. *Nanomaterials* **2023**, *13*, 1367. https://doi.org/10.3390/nano13081367

Academic Editor: Jakob Birkedal Wagner

Received: 24 March 2023
Revised: 7 April 2023
Accepted: 12 April 2023
Published: 14 April 2023

1. Introduction

To form active regions of visible LEDs for solid-state lighting, a large number of solutions has been suggested, including [1,2]. Among them, indium gallium nitride (InGaN) alloys have become of special importance due to demonstrated high emission efficiency, compatibility with conventional epitaxial techniques, and covering the major part of the visible spectral range [3–7]. First of all, this was due to a high internal quantum efficiency (IQE), attributed to the lateral electron and hole localization originating from fluctuation of either composition [8] or width of InGaN quantum wells (QWs) embedded in the active region [9]. Another evident reason was the possibility to cover the whole visible spectrum range by engineering the In content in the QWs [10,11].

However, this material system still faces some problems. First, the efficiency decreases in the green and yellow/amber spectral range, as compared to the blue one (the phenomenon known as "green gap"), which is still under investigation [12–14]. Second, the relevant lattice constant mismatch (≈10%) between InN and GaN makes a pseudomorphic growth of QWs with high In content problematic due to strain relaxation [15], enhanced indium segregation [16], enhanced fluctuations of QW widths, and InGaN

composition [17,18], since these factors favor likely generation of dislocations and other defects in the active region, reducing IQE of the LEDs [19]. Finally, InGaN/GaN wurtzite heterostructures, conventionally grown along the [0001] direction, exhibit strong built-in electric fields inside the QWs, producing a relevant quantum-confined Stark effect (QCSE): a tilt of the conduction and valence bands resulted in a reduced overlap of electron and hole wave functions and, eventually, in a decrease of the efficiency of radiative recombination in the LED [20–23].

A possible workaround of the above problems is the fabrication of quantum-dot-based active regions, which can be grown with a higher In content compared to QWs, due to reduction of the accumulated elastic energy via defect-free stress relaxation at the edges of the dots. This solution would also make it possible to extend the spectral range of InGaN-based LEDs, being limited by the bandgaps of binary compounds InN and GaN [10,11]. The quantum dots (QDs), i.e., the InGaN islands embedded in the GaN matrix, can be manufactured, in particular, by using a technologically controlled growth interruption technique once a 2D InGaN layer has been formed [24].

Several models have been suggested to study the electronic structure of wurtzite In_xGa_{1-x} N QDs including the effect of electromechanical field. The models use both the continuous approach, starting from the paper by Winkelnkemper et al. [25], who extended the model of Chuang and Chang [26], and atomistic simulations, which are supposed to include the real symmetry of the structure, such as a tight-binding model accounting for electromechanical fields in In_xGa_{1-x} N/GaN QDs [27], GaN/AlN QDs [28], and pure InN/GaN QDs [29].

Some papers from our group and coauthors have recently shown that accounts of the realistic strain distribution [30] and quantum confinement [31,32] in a nanostructure are fundamental for the accurate theoretical predictions and interpretation of experimental results. In this context, we have already presented a realistic model of an InGaN/GaN LED structure given by a thick n-GaN contact layer, a prelayer made of a 12-period short-period InGaN/GaN superlattice (SPSL), undoped GaN spacer, active region (AR) including double-stacked QD layers, p-AlGaN electron-blocking layer (EBL), and p-GaN contact layer. The model was quite suitable for studying the impact of the lateral and vertical QD coupling via electromechanical field [33] and possible extension of the wavelength emission range [34].

The present paper is aimed at analyzing the influence of InGaN compositional inhomogeneity in the QD on its optical properties. In fact, this aspect has been studied in quantum wells and more specifically in LED-based InGaN quantum-wells [35–38]. However, we are not yet aware of any publications that would thoroughly investigate this phenomenon in QDs, where it could significantly influence the quantum confinement of carriers and spatial localization of their wave functions. For this purpose, we applied both continuum models based on the $\vec{k} \cdot \vec{p}$ approach [39,40] and the atomistic model based on empirical tight-binding calculations [41,42] within a multiscale approach [43].

The paper is organized in the following way. In Section 2, we describe the procedure for generation of the two- and three-dimensional QD structures to be used in simulations. The models applied are considered in detail in Section 3. The results of simulations are discussed in Section 4, whereas our conclusions complete the paper.

2. Structures for Quantum Dots

The active region of the structure under study contains a double layer of InGaN islands formed by the growth-interruption approach. It is sandwiched between a 12 × {1 nm GaN/1 nm InGaN} period superlattice and undoped GaN spacer from the bottom side and a p-AlGaN electron blocking layer covered by a p-GaN contact layer from the top surface side.

Two- and three-dimensional reconstruction of the simulated QD structure was based on a special algorithm operating with an experimental image of the out-of-plane strain derived by the geometric phase analysis (GPA) of the high-resolution transmission electron

microscopy (HRTEM) image of a real QD structure [44]. The sample used for this purpose, as was already mentioned, contained several InGaN/GaN superlattices and large InGaN QD islands with the sizes of tens nanometers and nonuniform InGaN composition distribution.

For the present study, we sampled a single QD from the active region using the GwyddyonTM software [45], and then we reconstructed the two- and three-dimensional structures for simulation. The latter one was obtained within a rotation-invariance approximation, i.e., by rotation of two-dimensional structure around the hexagonal axis of the crystal. We suppose that such a three-dimensional structure was not far from the experimental one exhibiting a hexagonal or dodecagonal symmetry. The reconstruction method was described in detail in Ref. [31]. A finite element method (FEM) was subsequently applied to the reconstructed structures in order to discretize the electromechanical, electronic, and optical models. The entire experimental procedure for deriving the experimental out-of-plane strain distribution by the GPA of the QD HRTEM image and then extracting the reconstructed structures by a special algorithm was described and discussed in detail in Ref. [33].

The two-dimensional image of the out-of-plane strain of the experimental sample, from which two- and three-dimensional simulations structures were obtained, is shown in Figure 1. This sample was also used in our previous publications on the electromechanical coupling and wavelength emission range [33,34].

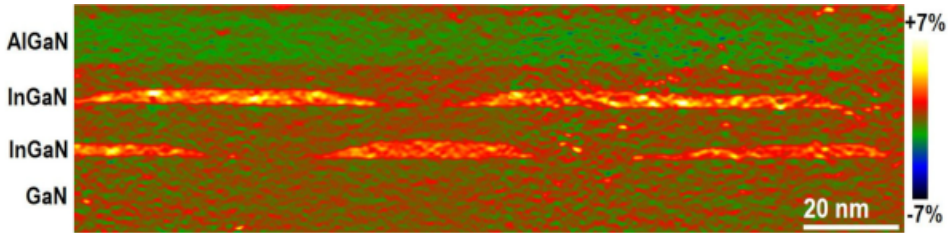

Figure 1. The two-dimensional image of the out-of-plane strain obtained by geometric phase analysis of the HRTEM image used to derive the three-dimensional structure.

3. Models

Calculations of the electromechanical fields were made according to the theories described in detail in Ref. [46]. In the continuum models, the total free energy density is used to derive the governing equations for the electromechanical fields of the crystal based on Newton's second law and Maxwell–Poisson equation, i.e., a set of four coupled equations for the electromechanical fields. The results were then used in the framework of the $\vec{k} \cdot \vec{p}$ model via deformation potentials [47].

In the atomistic approach, the valence-force-field (VFF) model provided the equilibrium atomic positions by minimizing the QD elastic energy, taking into account bond stretching and bond bending forces. The strain effects were then included in the empirical tight-binding (ETB) model with the Harrison-type scaling laws for fitted exponents [48].

The piezoelectric field was included directly in the continuum model, whereas it was calculated by a semicoupled model from the VFF results, which did not account for long-ranging Coulomb effects. Nevertheless, the atomistic VFF method and continuous model showed an excellent agreement with each other in the case of the strain field calculations for relatively large QDs [46,49].

Since our study is largely focused on investigating the impact of InGaN composition fluctuations in QDs on their emission spectra, we used single-particle models for band structure, neglecting Coulomb coupling and possible decoherence effects due to phonons [50]. In the continuum approach, the band structure calculations were based on the 8-band $\vec{k} \cdot \vec{p}$ model [39,40], which described electron, heavy-hole, light-hole, and spin-orbit split-off bands around the Γ point of the Brillouin zone, all other bands being considered as remote ones. The Hamiltonian is derived by Foreman's application of Burt's envelope function

for heterostructures [51,52]. The necessary band structure parameters were borrowed from Ref. [53].

Within this approach, the wave function of a state n with energy E_n was represented as a linear combination of eight Bloch magnitudes weighted by the respective envelope functions,

$$\psi_n = \sum_{i=1}^{8} \phi_i u_i, \tag{1}$$

where ϕ_i are the envelope function and u_i are the Bloch magnitudes [54]. We solved the $\vec{k} \cdot \vec{p}$ equations using the finite element method (FEM), accounting for the electromechanical field. Following the continuum approach, for the computation of optical transitions since the dipole matrix elements $\vec{\mu}_{nm}$ are ill defined in crystals involving extended Bloch states [52], these were calculated from the momentum matrix element

$$\begin{aligned} \vec{p}_{nm} &\equiv \langle \psi_n | \vec{p} \, | \psi_m \rangle \\ &= \sum_{i,j=1}^{8} \left(\langle \phi_i^{(n)} | \vec{p} \, | \phi_j^{(m)} \rangle \delta_{ij} + \langle \phi_i^{(n)} | \phi_j^{(m)} \rangle \langle u_i | \vec{p} \, | u_j \rangle \right) \\ &\equiv \vec{p}_{nm}^{(\phi)} + \vec{p}_{nm}^{(u)}, \end{aligned} \tag{2}$$

where $\vec{p}^{\,(\phi)}$ and $\vec{p}^{\,(u)}$ are the envelope and the Bloch constituents of the momentum matrix element, respectively. The envelope functions were usually slowly varying at the scale of the primitive cell, so it was possible to neglect them [55,56]. The oscillator strengths were finally given by [57]:

$$\vec{P}_{nm} = \frac{2\pi e^2 \hbar^2}{\epsilon_0 m_0^2 V} |\hat{e} \cdot \vec{p}_{nm}|^2, \tag{3}$$

where $\hat{e}$ is the direction unit vector of the electric field, V is the volume of the structure, e is the electron charge, m_0 is the free electron mass, and ϵ_0 is the vacuum permittivity.

The ETB method is usually based on precomputed parameters for the two-center interactions between the atomic orbitals [41]. Our model uses a parameterization based on a $sp^3s^*d^5$ local basis, as established in Ref. [48], where the parameters are fitted to experimental data and bulk dispersions obtained by density functional theory. The spin-orbit coupling is included within each atomic center [58].

Considering ETB optical transitions, we followed the work of Ref. [59], where momentum matrix elements are evaluated as

$$\vec{p}_{nm}(k) = \frac{m_0}{\hbar} \sum_{b\alpha b'\alpha'} C_{nk}^*(b,\alpha) C_{mk}(b',\alpha') \nabla_k H_{b\alpha,b'\alpha'(k)}, \tag{4}$$

where n, m are eigenstate indices while b, α denotes an atomic orbital α centered at $\vec{R}_b$, and in the momentum representation $\vec{\nabla}_{\vec{k}} H_{b\alpha,b'\alpha'(k=0)} = (\vec{R}_b - \vec{R}_{b'})$. The Equation (4) neglected intra-atomic terms and spin-orbit corrections. Generally, it is still controversial as to how optical transitions should be treated in the ETB approximation. Therefore, we refer one to the existing literature for a more detailed discussion [60–63]. All models were implemented and solved by using the TiberCAD simulator [64,65].

4. Results

A preliminary comparison of the experimentally measured strain field ε_{zz} relative to the GaN substrate with the predictions of the continuum model allowed us to obtain the actual average In content of the dots, which was estimated to be approximately 19%. Having established this fact, the first step of our study was to qualitatively analyze the

impact of local In content on the optical properties of an InGaN QD, comparing four different two-dimensional models.

The first two cases considered are (i) QD with a uniform In content of 19% in the whole structure and (ii) QD with a realistic nonuniform In content distribution given by the data, obtained with an ad hoc algorithm reconstructing the actual local alloy composition. The corresponding In composition profiles are shown in Figure 2.

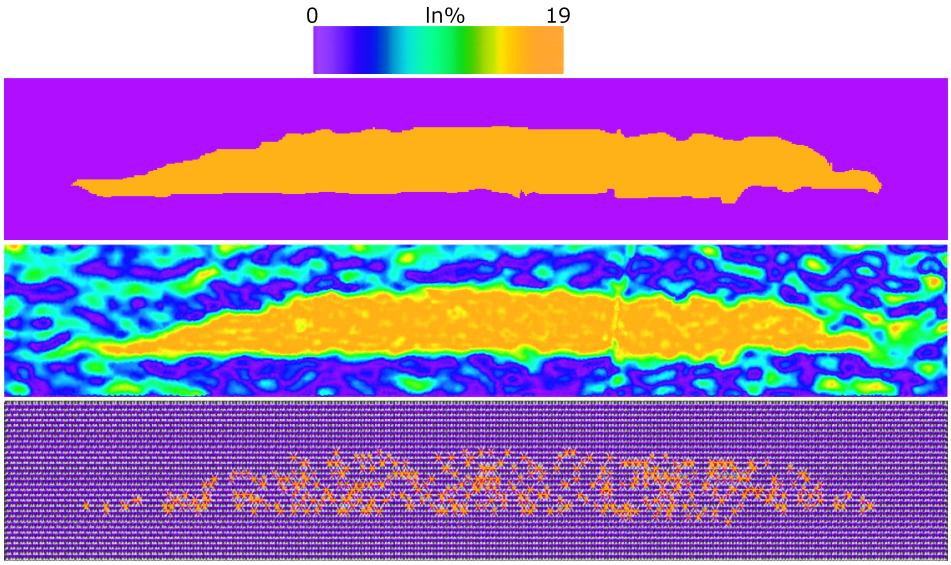

Figure 2. Two-dimensional distributions of the In content in the QD. (**Top**): the structure with a uniform In distribution of (19%). (**Center**): the structure derived by an algorithm accounting for the experimental local In content. (**Bottom**): the structure with an atomistic homogeneous random In distribution in InGaN QD with the mean content of 19% (bigger orange spots correspond to In atoms).

The simulations for these two configurations were performed with a continuum model for the electromechanical field [46] and 8-band $\vec{k} \cdot \vec{p}$ model for optoelectronic properties [40]. The strain distribution inside the QD is closely related to the local In content. In the case of a uniform In distribution in the QD, the strain field is also highly uniform and rapidly tends to zero outside the QD. In the case of the real (experimental) In content distribution, the strain fluctuates inside the QD and does not disappear outside of the dot, where the In content is still nonzero [33].

For the last two cases, we considered results obtained by the ETB model with sp3d5s* parameterization [41,42] and atomistic strain field calculated by the VFF method [66], which allow for modeling, in detail, the real indium distributions on the atomic scale. Here, the local strain was also included in the simulations in order to obtain more accurate electronic band structures [37,67]. We implemented two different atomistic approximations in order to include the effect of local InGaN composition fluctuations: the virtual crystal approximation (VCA) and the random alloy (RA) approach. VCA considers an ABC alloy as a fictitious material whose properties are a weighted average of the properties of binary constituents AC and BC, according to Vegard's law [68]. RA uses the properties averaging over numerous stochastic configurations where the anion A occupies a lattice site with the probability equal to its molar fraction in the alloy. Here, we considered 30 different random configurations within the RA approach. In the bottom of Figure 2, we plot one of the RA configurations, corresponding to the mean 19% In content.

Figure 3 presents two-dimensional ground-state (GS) wave functions of electrons (adjacent to the top boundary of QD) and holes (adjacent to the bottom boundary of QD).

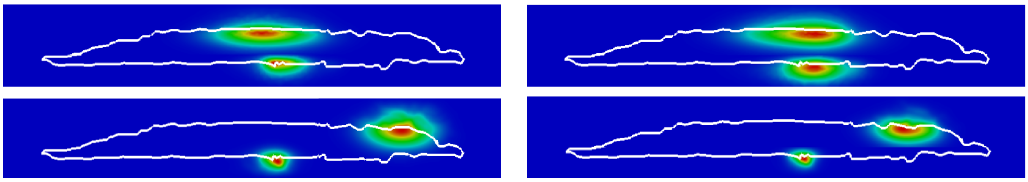

Figure 3. Simulations with two-dimensional models. (**Top**): GS for electrons and holes in the case of $\vec{k} \cdot \vec{p}$ for uniform In content (**left**) and VCA (**right**). (**Bottom**): GS for electrons and holes in the case of $\vec{k} \cdot \vec{p}$ for real In content (**left**) and for one RA configuration (**right**).

Such an adjacency originates from the well-known QCSE in a wurtzite-symmetry structure, since the electric field due to spontaneous polarization and piezoelectric effect shifts the electron and hole wave functions to the opposite sides of the QDs [20–23,33]. All the panels in the figure demonstrate the localization of the carrier probability densities. However, the localization character is quite different in the cases of (i) the $\vec{k} \cdot \vec{p}$ model with uniform In content distribution or VCA approach and (ii) the $\vec{k} \cdot \vec{p}$ model with real In content distribution or RA approach. In the former case, the electron and hole wave functions are localized in the most wide region of the InGaN QD where the carriers exhibit a weaker quantum confinement. There, the asymmetry of the wave functions and their localization radii are influenced by particular local fluctuations of the QD width. In the latter case, the electron wave function is localized near the edge of the QD, being controlled by local fluctuations of both QD width and composition; the hole localization is nearly the same as in the former case.

To exclude the artifacts that may be an effect of a two-dimensional quantization, we repeated all the simulations using a three-dimensional structure of the QD instead of a two-dimensional one. The corresponding GS wave functions of electrons and holes are shown in Figure 4.

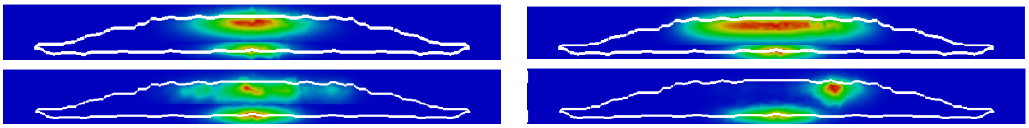

Figure 4. Simulations with three-dimensional models. (**Top**): GS for electrons and holes in the case of $\vec{k} \cdot \vec{p}$ for uniform In content (**left**) and VCA (**right**). (**Bottom**): GS for electrons and holes in the case of one RA configuration in the xz (**left**) and yz (**right**) planes.

The results obtained do not differ remarkably from those obtained by two-dimensional models. Again, the results coming from the $\vec{k} \cdot \vec{p}$ model with uniform In content distribution and from the VCA approach are similar to each other and differ from the two-dimensional results only by the lateral extensions of the electron and hole wave functions (as previously, all the wave functions were located in the widest part of the QD). The RA approach provides qualitatively different characters of carrier localization, with electrons to be localized aside the central part of the QD. Since we do not have an experimental three-dimensional distribution of the In content available, it was not possible to perform a $\vec{k} \cdot \vec{p}$ calculation for this case.

The above results enable us to make an important conclusions. The trends of electron and hole localization depend substantially on particular InGaN composition distribution in the QD. Therefore, the account of realistic In content distribution is a fundamental aspect, regardless of the model and the choice of a two- or three-dimensional QD structure.

The localization of carriers affects the optical properties of the QD. It is to be expected that the models with a uniform InGaN composition distribution, i.e., continuous ($\vec{k} \cdot \vec{p}$ model and VCA, would present similar overlaps of the electron and hole wave functions and, thus, comparable optical strengths. On the contrary, the results given by the $\vec{k} \cdot \vec{p}$ model with experimental local In content distribution and ETB with random-alloy atomic

distribution, which mimics a realistic In content, would show a reduction in the overlaps and, consequentially, in the intensities of the optical strengths.

This is exactly what we see in Figure 5, where the optical strengths for all the two-dimensional cases given by the $\vec{k} \cdot \vec{p}$ model with uniform and experimental In content distributions and those obtained by ETB model within VCA and RA approximation are plotted as a function of the optical transition energy. Dependence of the electron and hole states on the local InGaN composition fluctuations and different spatial localization of the carrier wave functions, which are accounted for by the $\vec{k} \cdot \vec{p}$ and ETB models with real In content distribution, results in much lower, approximately by a factor of ten, magnitudes of the optical strengths compared to those assumed to have a uniform distribution. Furthermore, VCA with a linear interpolation of the bandgap considerably overestimates the transition energy [38], whereas the $\vec{k} \cdot \vec{p}$ model with uniform In content underestimates it, as it considers the In content to be systematically greater than the real one, providing an incorrect quantum confinement.

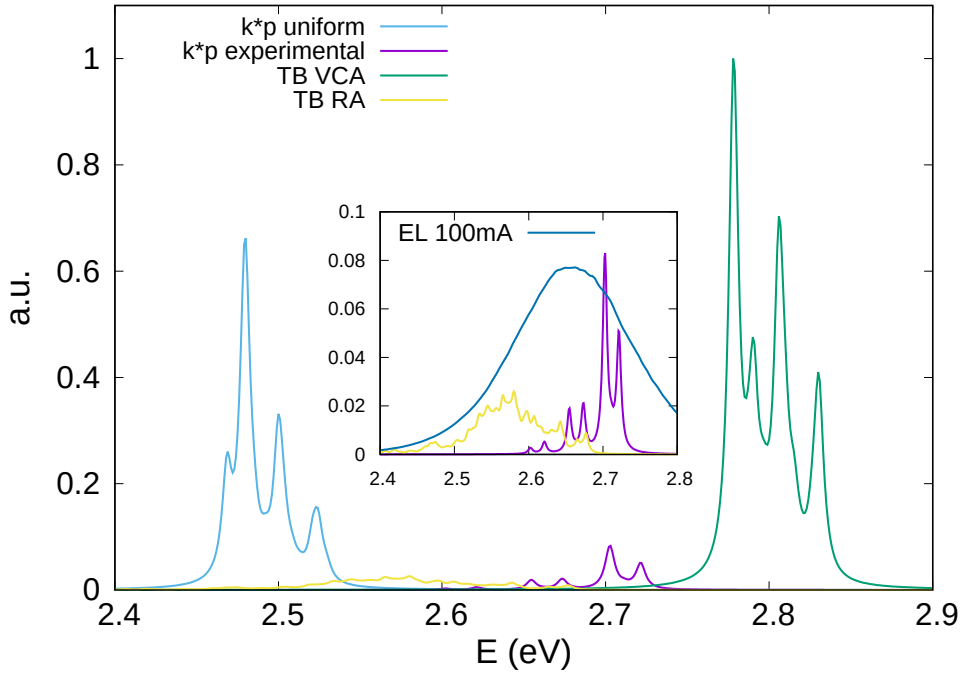

Figure 5. Optical strengths as a function of optical transition energy given by the $\vec{k} \cdot \vec{p}$ models with uniform and real In content distributions and by the ETB approach with VCA and RA composition distributions.

The inset in Figure 5 shows the comparison of our simulations with the experimental room-temperature electroluminescence (EL) spectrum obtained from the studied QD LED structure [33]. The following observations can be made from the comparison. First, one can see that the peak of the experimental EL spectrum is red-shifted by about 60 meV with respect to the principal double-peak of the optical strength obtained with the real In content distribution in the structure and zero temperature. This value is close to the red shift of 65 meV that corresponded to the temperature rise from zero to 300 K and was estimated by the experimental Varshni parameters reported for GaN and InN and bowing parameter for the bandgap of the InGaN alloy. Second, the optical strength spectrum calculated for RA configurations lies well below the above double peak obtained by the $\vec{k} \cdot \vec{p}$ model with the real In content distribution, and likely forms the low-energy wing of the experimental EL spectrum. This may be attributed to the fact that 30 different configurations were accounted for to obtain the optical strength spectra in the RA ETB model, whereas the only InGaN composition distribution averaged over the thickness of the sample studied by TEM was used for realistic $\vec{k} \cdot \vec{p}$ calculations. From such a point of view, the realistic $\vec{k} \cdot \vec{p}$ and RA

tight-binding calculations should be regarded as complementary rather then alternative. In particular, the RA calculations may quantitatively explain a wide low-energy wing of the experimental EL spectrum, associating it with InGaN composition fluctuations inherent in RA. In general, both realistic $\vec{k} \cdot \vec{p}$ and RA simulations quite accurately predict the spectral extent of the optical strength. Therefore, account of the local realistic parameters is vital for this kind of simulation, regardless of whether using an atomistic or a continuous method. In this context, a future development of our model will combine the local distribution of a material given by experimental data with the atomic distribution, in order to reduce the statistical fluctuations of the RA model.

5. Conclusions

We reported on continuum and atomistic models of optoelectronic properties of a single QD, exploiting two- and three-dimensional QD structures derived from an HRTEM image with nonuniform InGaN composition distribution inside. We compared continuous and atomistic simulations with uniform (mean) and nonuniform (real) In content distributions, analyzing the impact of the local In content on optical properties of the QD.

We found different characters of GS electron and hole localization inside the QD. In the models with a uniform distribution, electrons and holes are localized in the widest regions of the QD, being primarily controlled by the width fluctuations. In the models with nonuniform distribution, fluctuations of the InGaN composition in the QD are likely the main reason for localization of electrons and holes in spatially different regions of the QD.

These different carrier localizations result immediately in a much lower magnitude of the optical transition strengths calculated with accounting of the nonuniform In content distribution compared to the the uniform case. Moreover, the VCA atomistic model is found to overestimate the energies of optical transitions in the QD. In contrast, the $\vec{k} \cdot \vec{p}$ model with a uniform mean In content leads to underestimation of the optical-transition energies. Comparison of the optical strength distributions obtained by both the $\vec{k} \cdot \vec{p}$ model utilizing the real In content distribution and the atomistic ETB model within RA approximation and experimental emission spectrum demonstrated their reasonable agreement. This shows that accounting for the local composition fluctuations in InGaN QDs is the principal and important aspect for this kind of simulation, regardless of the use of either atomistic or continuous models.

Author Contributions: D.B.: Conceptualization, investigation, numerical calculation, writing—original draft preparation, writing—review and editing, funding acquisition. A.V.S.: Investigation, writing—review and editing. A.F.T.: Investigation, writing—review and editing. A.E.N.: Investigation, writing—review and editing. A.P.: Investigation, writing—review and editing. M.A.d.M.: Investigation, writing—review and editing. S.Y.K.: Investigation, writing—review and editing. N.C.: Investigation, writing—review and editing, funding acquisition. All authors have read and agreed to the published version of the manuscript.

Funding: This research was funded by the French National Research Agency under the "Investissement 'Avenir" program reference No. ANR-10-EQPX-38-01 and ATHENA-European University (EPLUS2020-AG, Project 101004096).

Data Availability Statement: The data presented in the current work are available on request from corresponding authors.

Conflicts of Interest: The authors declare no conflict of interest.

Abbreviations

The following abbreviations are used in this manuscript:

LED	Light-emitting diode
QWs	Quantum wells
QDs	Quantum dots
AR	Active region
IQE	External quantum efficiency
QCSE	Quantum-confined Stark effect
SPSL	Short-period superlattice
EBL	Electron blocking layer
GPA	Geometric phase analysis
HRTEM	High-resolution transmission electron microscopy
FEM	Finite element model
VFF	Valence force field
ETB	Empirical tight-binding
VCA	Virtual crystal approximation
RA	Random alloy

References

1. Yin, W.; Bai, X.; Zhang, X.; Zhang, J.; Gao, X.; Yu, W.W. Multicolor Light-Emitting Diodes with MoS_2 Quantum Dots. *Part. Part. Syst. Charact.* **2019**, *36*, 1800362. [CrossRef]
2. Elahi, E.; Farooq Khan, M.F.; Rehman, S.; Khalil, H.M.W.; Rehman, M.A.; Kim, D.-k.; Kim, H.; Khan, K.; Shahzad, M.; Iqbal, M.W.; et al. Enhanced electrical and broad spectral (UV-Vis-NIR) photodetection in a Gr/$ReSe_2$/Gr heterojunction. *Dalton Trans.* **2020**, *49*, 10017–10027. [CrossRef]
3. Nakamura, S.; Mukai, T.; Senoh, M. Candela-class high-brightness InGaN/AlGaN double-heterostructure blue-light-emitting diodes. *Appl. Phys. Lett.* **1994**, *64*, 1687. [CrossRef]
4. Nakamura, S.; Senoh, M.; Iwasa, N.; Nagahama, S.I. High-power InGaN single-quantum-well-structure blue and violet light-emitting diodes. *Appl. Phys. Lett.* **1995**, *67*, 1868. [CrossRef]
5. Amano, H.; Kito, M.; Hiramatsu, K.; Akasaki, I. P-Type Conduction in Mg-Doped GaN Treated with Low-Energy Electron Beam Irradiation (LEEBI). *J. Appl. Phys.* **1989**, *28*, 21122114. [CrossRef]
6. Pimputkar, S.; Speck, J.S.; DenBaars, S.P.; Nakamura, S. Prospects for LED lighting. *Nat. Photonics* **2009**, *3*, 180–182. [CrossRef]
7. Horiuchi, N. Natural white light. *Nat. Photonics* **2010**, *4*, 738. [CrossRef]
8. Chichibu, S.F.; Abare, A.C.; Minsky, M.S.; Keller, S.; Fleischer, S.B.; Bowers, J.E.; Hu, E.; Mishra, U.K.; Coldren, L.A.; DenBaars, S.P. Effective band gap inhomogeneity and piezoelectric field in InGaN/GaN multiquantum well structures. *Appl. Phys. Lett.* **1998**, *73*, 2006. [CrossRef]
9. Zhou, X.; Yu, E.T.; Florescu, D.; Ramer, J.C.; Lee, D.S.; Armour, E.A. Observation of subsurface monolayer thickness fluctuations in InGaN/GaN quantum wells by scanning capacitance microscopy and spectroscopy. *Appl. Phys. Lett.* **2004**, *85*, 407. [CrossRef]
10. Banerjee, A.; Dogan, F.; Heo, J.; Manchon, A.; Guo, W.; Bhattacharya, P. Spin Relaxation in InGaN Quantum Disks in GaN Nanowires. *Nano Lett.* **2011**, *11*, 5396–5400. [CrossRef]
11. Lin, H.W.; Lu, Y.J.; Chen, H.Y.; Lee, H.M.; Gwo, S. InGaN/GaN nanorod array white light-emitting diode. *Appl. Phys. Lett.* **2010**, *97*, 073101. [CrossRef]
12. O'Donnell, K.P.; Auf der Maur, M.; Di Carlo, A.; Lorenz, K.; the SORBET consortium. It's not easy being green: Strategies for all-nitrides, all-colour solid state lighting. *Phys. Status Solidi RRL* **2012**, *6*, 49–52. [CrossRef]
13. Krames, M.R.; Shchekin, O.B.; Mueller-Mach, R.; Mueller, G.O.; Zhou, L.; Harbers, G.; Craford, M.G. Status and Future of High-Power Light-Emitting Diodes for Solid-State Lighting. *J. Display Technol.* **2007**, *3*, 160–175. [CrossRef]
14. Park, I.K.; Kwon, M.K.; Kim, J.O.; Seo, S.B.; Kim, J.Y.; Lim, J.H.; Park, S.J. Green light-emitting diodes with self-assembled In-rich InGaN quantum dots. *Appl. Phys. Lett.* **2007**, *91*, 133105. [CrossRef]
15. Kim, C.S.; Kim, H.G.; Hong, C.-H.; Cho, H.K. Effect of compressive strain relaxation in GaN blue light-emitting diodes with variation of n^+-GaN thickness on its device performance. *Appl. Phys. Lett.* **2005**, *87*, 013502. [CrossRef]
16. Suski, T.; Franssen, G.; Kamińska, A.; Khachapuridze, A.; Teisseyre, H.; Plesiewicz, J.A.; Dmowski, L.H.; Lu, H.; Schaff, W.J.; Kurouchi, M.; et al. The influence of alloy disorder and hydrostatic pressure on electrical and optical properties of In-rich InGaN compounds. *Proc. SPIE* **2007**, *6473*, 647311. [CrossRef]
17. Laukkanena, P.; Lehkonena, S.; Uusimaaa, P.; Pessaa, M.; Seppäläb, A.; Ahlgrenb, T.; Rauhalab, E. Emission studies of InGaN layers and LEDs grown by plasma-assisted MBE. *J. Cryst. Growth* **2001**, *230*, 503. [CrossRef]
18. Chiu, C.H.; Lu, T.C.; Huang, H.W.; Lai, C.F.; Kao, C.C.; Chu, J.T.; Yu, C.C.; Kuo, H.C.; Wang, S.C.; Lin, C.F.; et al. Fabrication of InGaN/GaN nanorod light-emitting diodes with self-assembled Ni metal islands. *Nanotechnology* **2007**, *18*, 445201. [CrossRef]
19. Cho, H.K.; Lee, J.Y.; Kim, C.S.; Yang, G.M. Influence of strain relaxation on structural and optical characteristics of InGaN/GaN multiple quantum wells with high indium composition. *J. Appl. Phys.* **2002**, *91*, 1166. [CrossRef]

20. Waltereit, P.; Brandt, O.; Trampert, A.; Grahn, H.T.; Menniger, J.; Ramsteiner, M.; Reiche, M.; Ploog, K.H. Nitride semiconductors free of electrostatic fields for efficient white light-emitting diodes. *Nature* **2000**, *406*, 865. [CrossRef]
21. Shapiro, N.A.; Feick, H.; Hong, W.; Cich, M.; Armitage, R.; Weber, E.R. Luminescence energy and carrier lifetime in InGaN/GaN quantum wells as a function of applied biaxial strain. *J. Appl. Phys.* **2003**, *94*, 4520. [CrossRef]
22. Li, S.; Ware, M.; Wu, J.; Minor, P.; Wang, Z.; Wu, Z.; Jiang, Y.; Salamo, G.J. Polarization induced pn-junction without dopant in graded AlGaN coherently strained on GaN. *Appl. Phys. Lett.* **2012**, *101*, 122103. [CrossRef]
23. Li, S.; Ware, M.E.; Wu, J.; Kunets, V.P.; Hawkridge, M.; Minor, P.; Wang, Z.; Wu, Z.; Jiang, Y.; Salamo, G.J. Polarization doping: Reservoir effects of the substrate in AlGaN graded layers. *J. Appl. Phys.* **2012**, *112*, 053711. [CrossRef]
24. Tsatsulnikov, A.F.; Lundin, W.V.; Sakharov, A.V.; Nikolaev, A.E.; Zavarin, E.E.; Usov, S.O.; Yagovkina, M.A.; Hÿtch, M.J.; Korytov, M.; Cherkashin, N. Formation of Three-Dimensional Islands in the Active Region of InGaN Based Light Emitting Diodes Using a Growth Interruption Approach. *Sci. Adv. Mater.* **2015**, *7*, 1629–1635. [CrossRef]
25. Winkelnkemper, M.; Schliwa, A.; Bimberg, D. Interrelation of structural and electronic properties in $In_xGa_{1-x}N$/GaN quantum dots using an eight-band $k \cdot p$ model. *Phys. Rev. B* **2006**, *74*, 155322. [CrossRef]
26. Chuang, S.L.; Chang, C.S. $k \cdot p$ method for strained wurtzite semiconductors. *Phys. Rev. B* **1996**, *54*, 2491. [CrossRef]
27. Saitoa, T.; Arakawa, Y. Electronic structure of piezoelectric $In_{0.2}Ga_{0.8}N$ quantum dots in GaN calculated using a tight-binding method. *Phys. E* **2002**, *15*, 169. [CrossRef]
28. Ranjan, V.; Allan, G.; Priester, C.; Delerue, C. Self-consistent calculations of the optical properties of GaN quantum dots. *Phys. Rev. B* **2003**, *68*, 115305. [CrossRef]
29. Baer, N.; Schulz, S.; Schumacher, S.; Gartner, P.; Czycholl, G.; Jahnke, F. Optical properties of self-organized wurtzite InN/GaN quantum dots: A combined atomistic tight-binding and full configuration interaction calculation. *Appl. Phys. Lett.* **2005**, *87*, 231114. [CrossRef]
30. Lassen, B.; Barettin, D.; Willatzen, M. Strain in inhomogeneous InAs/GaAs quantum dot structures. *J. Phys. Conf. Ser.* **2012**, *367*, 012007. [CrossRef]
31. Barettin, D.; De Angelis, R.; Prosposito, P.; Auf der Maur, M.; Casalboni, M.; Pecchia, A. Model of a realistic InP surface quantum dot extrapolated from atomic force microscopy results. *Nanotechnology* **2014**, *25*, 195201. [CrossRef] [PubMed]
32. Barettin, D.; De Angelis, R.; Prosposito, P.; Auf der Maur, M.; Casalboni, M.; Pecchia, A. Inter-dot strain field effect on the optoelectronic properties of realistic InP lateral quantum-dot molecules. *J. Appl. Phys.* **2015**, *117*, 094306. [CrossRef]
33. Barettin, D.; Auf Der Maur, M.; di Carlo, A.; Pecchia, A.; Tsatsulnikov, A.F.; Sakharov, A.V.; Lundin, W.V.; Nikolaev, A.E.; Usov, S.O.; Cherkashin, N.; et al. Influence of electromechanical coupling on optical properties of InGaN quantum-dot based light-emitting diodes. *Nanotechnology* **2017**, *28*, 015701. [CrossRef] [PubMed]
34. Barettin, D.; Auf Der Maur, M.; di Carlo, A.; Pecchia, A.; Tsatsulnikov, A.F.; Lundin, W.V.; Sakharov, A.V.; Nikolaev, A.E.; Korytov, M.; Cherkashin, N.; et al. Carrier transport and emission efficiency in InGaN quantum-dot based light-emitting diodes. *Nanotechnology* **2017**, *28*, 275201. [CrossRef]
35. Auf Der Maur, M.; Barettin, D.; Pecchia, A.; Sacconi, F.; Di Carlo, A. Effect of alloy fluctuations in InGaN/ GaN quantum wells on optical emission strength. In Proceedings of the International Conference on Numerical Simulation of Optoelectronic Devices (NUSOD), Mallorca, Spain, 1–4 September 2014; pp. 11–12. [CrossRef]
36. Auf der Maur, M.; Pecchia, A.; Penazzi, G.; Rodrigues, W.; Di Carlo, A. Efficiency Drop in Green InGaN \GaN Light Emitting Diodes: The Role of Random Alloy Fluctuations. *Phys. Rev. Lett.* **2016**, *116*, 027401. [CrossRef]
37. Lopez, M.; Pecchia, A.; Auf der Maur, M.; Sacconi, F.; Penazzi, G.; Di Carlo, A. Atomistic simulations of InGaN/GaN random quantum well LEDs. *Phys. Status Solidi C* **2014**, *11*, 632–634. [CrossRef]
38. Lopez, M.; Auf der Maur, M.; Pecchia, A.; Sacconi, F.; Penazzi, G.; Di Carlo, A. Simulation of random alloy effects in InGaN/GaN LEDs. In Proceedings of the 13th International Conference on Numerical Simulation of Optoelectronic Devices (NUSOD), Vancouver, BC, Canada, 19–22 August 2013; pp. 113–114. [CrossRef]
39. Lew Yan Voon, L.C.; Willatzen, M. *The $k \cdot p$ Method: Electronic Properties of Semiconductors*; Springer: Berlin/Heidelberg, Germany, 2009.
40. Barettin, D.; Pecchia, A.; Auf der Maur, M.; Di Carlo, A.; Lassen, B.; Willatzen, M. Electromechanical field effects in InAs/GaAs quantum dots based on continuum k*p and atomistic tight-binding methods. *Comput. Mater. Sci.* **2021**, *197*, 110678. [CrossRef]
41. Di Carlo, A. Microscopic theory of nanostructured semiconductor devices: Beyond the envelope-function approximation. *Semicond. Sci. Technol.* **2003**, *18*, R1. [CrossRef]
42. Jancu, J.-M.; Bassani, F.; Della Sala, F.; Scholz, R. Transferable tight-binding parametrization for the group-III nitrides. *Appl. Phys. Lett.* **2002**, *81*, 4838. [CrossRef]
43. Auf der Maur, M.; Penazzi, G.; Romano, G.; Sacconi, F.; Pecchia, A.; di Carlo, A. The Multiscale Paradigm in Electronic Device Simulation. *IEEE Trans. Electron Devices* **2011**, *58*, 1425–1432. [CrossRef]
44. Hÿtch, M.; Snoeck, E.; Kilaas, R. Quantitative measurement of displacement and strain fields from HREM micrographs. *Ultramicroscopy* **1998**, *74*, 131. [CrossRef]
45. Gwyddion—Free SPM (AFM, SNOM/NSOM, STM, MFM) Data Analysis Software. Available online: http://gwyddion.net/ (accessed on 1 March 2023).
46. Barettin, D.; Madsen, S.; Lassen, B.; Willatzen, M. Computational Methods for Electromechanical Fields in Self-Assembled Quantum Dots. *Commun. Comput. Phys.* **2012**, *11*, 797–830. [CrossRef]

47. Bir, G.L.; Pikus, G.E. *Symmetry and Strain-Induced Effects in Semiconductors*; Wiley: New York, NY, USA, 1974; p. 295.
48. Jancu, J.-M.; Scholz, R.; Beltram, F.; Bassani, F. Empirical spds* tight-binding calculation for cubic semiconductors: General method and material parameters. *Phys. Rev. B* **1998**, *57*, 6493. [CrossRef]
49. Barettin, D.; Madsen, S.; Lassen, B.; Willatzen, M. Comparison of wurtzite atomistic and piezoelectric continuum strain models: Implications for the electronic band structure. *Superlatt. Microstruct.* **2010**, *47*, 134. [CrossRef]
50. Jacak, L.; Krasnyj, J.; Jacak, W.; Gonczarek, R.; Machnikowski, P. Unavoidable decoherence in semiconductor quantum dots. *Phys. Rev. B* **2005**, *72*, 245309. [CrossRef]
51. Foreman, B.A. Effective-mass Hamiltonian and boundary conditions for the valence bands of semiconductor microstructures. *Phys. Rev. B* **1993**, *48*, 4964. [CrossRef] [PubMed]
52. Burt, M.G. The evaluation of the matrix element for interband optical transitions in quantum wells using envelope functions. *J. Phys. Condens. Matter* **1993**, *5*, 4091. [CrossRef]
53. Vurgaftman, I.; Meyer, J.R.; Ram-Mohan, L.R. Band parameters for III–V compound semiconductors and their alloys. *J. Appl. Phys.* **2001**, *89*, 5815. [CrossRef]
54. Pokatilov, E.P.; Fonoberov, V.A.; Fomin, V.M.; Devreese, J.T. Development of an eight-band theory for quantum dot heterostructures. *Phys. Rev. B* **2001**, *64*, 245328. [CrossRef]
55. Schliwa, A.; Winkelnkemper, M.; Bimberg, D. Impact of size, shape, and composition on piezoelectric effects and electronic properties of In(Ga)As/GaAs quantum dots. *Phys. Rev. B* **2007**, *76*, 205324. [CrossRef]
56. Barettin, D.; Houmark, J.; Lassen, B.; Mørk, J.; Jauho, A.-P. Optical properties and optimization of electromagnetically induced transparency in strained InAs/GaAs quantum dot structures. *Phys. Rev. B* **2009**, *80*, 235304. [CrossRef]
57. Stier, O.; Grundmann, M.; Bimberg, D. Electronic and optical properties of strained quantum dots modeled by 8-band $k \cdot p$ theory. *Phys. Rev. B* **1999**, *59*, 5688. [CrossRef]
58. Chadi, D.J. Spin-orbit splitting in crystalline and compositionally disordered semiconductors. *Phys. Rev. B* **1977**, *16*, 790. [CrossRef]
59. Lew Yan Voon, L.C.; Ram-Mohan, L.R. Tight-binding representation of the optical matrix elements: Theory and applications. *Phys. Rev. B* **1993**, *47*, 15500. [CrossRef]
60. Graf, M.; Vogl, P. Electromagnetic fields and dielectric response in empirical tight-binding theory. *Phys. Rev. B* **1995**, *51*, 4940. [CrossRef] [PubMed]
61. Boykin, T.B.; Bowen, R.C.; Klimeck, G. Electromagnetic coupling and gauge invariance in the empirical tight-binding method. *Phys. Rev. B* **2001**, *63*, 245314. [CrossRef]
62. Sandu, T. Optical matrix elements in tight-binding models with overlap. *Phys. Rev. B* **2005**, *72*, 125105. [CrossRef]
63. Zielinski, M.; Korkusinski, M.; Hawrylak, P. Atomistic tight-binding theory of multiexciton complexes in a self-assembled InAs quantum dot. *Phys. Rev. B* **2010**, *81*, 085301. [CrossRef]
64. Masharin, M.A.; Berestennikov, A.S.; Barettin, D.; Voroshilov, P.M.; Ladutenko, K.S.; Di Carlo, A.; Makarov, S.V. Giant enhancement of radiative recombination in perovskite light-emitting diodes with plasmonic core-shell nanoparticles. *Nanomaterials* **2021**, *11*, 45. [CrossRef]
65. Semenova, E.; Kulkova, I.; Kadkhodazadeh, S.; Barettin, D.; Kopylov, O.; Cagliani, A.; Almdal, K.; Willatzen, M.; Yvind, K. Epitaxial growth of quantum dots on InP for device applications operating at the 1.55 μm wavelength range. *Proc. SPIE* **2014**, *8996*, 899606. [CrossRef]
66. Keating, P.N. Effect of Invariance Requirements on the Elastic Strain Energy of Crystals with Application to the Diamond Structure. *Phys. Rev.* **1966**, *145*, 637. [CrossRef]
67. Lopez, M.; Sacconi, F.; Auf der Maur, M.; Pecchia, A.; Di Carlo, A. Atomistic simulation of InGaN/GaN quantum disk LEDs. *Opt. Quant. Electron.* **2012**, *44*, 89–94. [CrossRef]
68. Vegard, L. Die Konstitution der Mischkristalle und die Raumfüllung der Atome. *Z. Phys.* **1921**, *5*, 17–26. [CrossRef]